Journal of Electronic Materials (2024) 53:5769–5775
https://doi.org/10.1007/s11664-024-11312-5

BRIEF COMMUNICATION

# Structural, Magnetic, and Magnetocaloric Effects of $La_{0.8}Sr_{0.2}MnO_3$ Manganites by Doping with *f*-Orbital Ions Through First-Principles Calculations

**Changji Xu[1] · Wenbin He[1] · Zhuojia Xie[1] · Zhengguang Zou[1,2]**

Received: 2 April 2024 / Accepted: 1 July 2024 / Published online: 24 July 2024


## Abstract

In this study, $La_{0.63}Sr_{0.2}Nd_{0.17}MnO_3$ was synthesized by the sol-gel method, and its structural, morphological, magnetic, and magnetocaloric effects were investigated. The structural properties were analyzed by x-ray diffraction (XRD), and scanning electron microscopy (SEM) was used to characterize the morphology. An integrated magnetic measurement system was used to determine the magnetic properties. $La_{0.63}Sr_{0.2}Nd_{0.17}MnO_3$ crystallized in a hexagonal crystal system with space group *R*-3*c*. This was also confirmed by Rietveld refinement of the x-ray data from $La_{0.63}Sr_{0.2}Nd_{0.17}MnO_3$. With the doping of $Nd^{3+}$, the cell volume decreases, which can be explained by the angles and bond lengths of the bonds between the Mn and O ions and the distortion of the lattice. Near the Curie temperature, $La_{0.63}Sr_{0.2}Nd_{0.17}MnO_3$ exhibits significant magnetocaloric effects. The magnetic study of $La_{0.63}Sr_{0.2}Nd_{0.17}MnO_3$ suggests that the transition from the paramagnetic to ferromagnetic phase can occur near the Curie temperature. The maximum magnetic entropy change and relative cooling power (RCP) of $La_{0.63}Sr_{0.2}Nd_{0.17}MnO_3$ (298 K, 3 T) are 2.70 J/(kg K) and 135 (J/kg), respectively. The effect of *f*-orbitals on the magnetic properties of $La_{0.8}Sr_{0.2}MnO_3$ was investigated by first-principles calculations in density functional theory. Thus, it can be concluded that the magnetocaloric effects of the material after doping with *f*-orbital ions ($Nd^{3+}$) is enhanced compared to $La_{0.8}Sr_{0.2}MnO_3$.

**Keywords** Magnetic · magnetocaloric effect · manganites · doping · first-principles calculations

## Introduction

Nowadays, global environmental problems are increasingly severe, and green environmental protection is the mainstream of future research and development. Compared to conventional gas refrigeration technology, magnetic refrigeration technology has gained increasing prominence because of its higher cooling efficiency and lower pollution.[1–6] Magnetic refrigeration materials with the advantages of stable performance, green environmental protection, and high refrigeration efficiency have garnered extensive attention from researchers. In recent years, a wide range of experimental and theoretical studies have been carried out on the magnetic properties and magnetocaloric effect (MCE) of many magnetic materials. The MCE is an intrinsic feature of magnetic materials, in which changes in magnetic entropy within a magnetic material caused by changes in an external magnetic field are accompanied by the absorption and release of heat.[7] In recent years, advanced results have been achieved with low-temperature magnetically cooled oxide materials,[8–10] which play an important role in the fields of aerospace and medicine, among others. However, magnetic refrigeration materials in the room-temperature or sub-room-temperature range have an irreplaceable role in life. To date, many magnetic solid materials (rare earth [RE]-based magnetic materials, $A_2B_2O_7$, $ABO_3$, rare earth oxychlorides, rare earth cobalt–nickel-based magneto-thermal

Changji Xu and Wenbin He contributed equally to this work.

✉ Zhengguang Zou
zouzgglut@163.com

✉ Zhuojia Xie
writerxie@163.com

[1] College of Materials Science and Engineering, Guilin University of Technology, Guilin 541004, China

[2] Collaborative Innovation Center for Exploration of Hidden Nonferrous Metal Deposits and Development of New Materials, Guilin University of Technology, Guilin 541004, China

materials, etc.) and alloy magneto-thermal materials related to rare earths have been studied. These materials have been found to exhibit excellent magneto-thermal properties.[11–15] Perovskite manganites have gained in popularity, as they are low-cost, have a very high $\Delta S_M$, and exhibit second-order magnetic phase transitions (SOMPT).[16–21] $LaMnO_3$ is a classical antiferromagnetic material. When doping ions of different valence states into the La site, mixed valence states $Mn^{3+}$ and $Mn^{4+}$ may appear, which further produces a double exchange (DE) through electron transfer between the adjacent ions $Mn^{3+}$ and $Mn^{4+}$ by $O^{2-}$.[22] Because of the important role of rare earth ions in magnetic materials, many researchers have employed the doping of rare earth ions based on $La_{1-x}Sr_xMnO_3$ (LSMO) to regulate the Curie temperature ($T_c$) of the material and to optimize the magneto-thermal effect of the material. In this paper, the magneto-thermal properties of LSMO are optimized by doping $Nd^{3+}$. Furthermore, doping of ions with *f*-orbitals ($Pr^{3+}$, $Nd^{3+}$, $Gd^{3+}$) to replace La sites can significantly increase the MCE of the material with a small reduction in DE.[23–27] Therefore, in this paper, the physical mechanism of $La_{0.8}Sr_{0.2}MnO_3$ and $La_{0.63}Sr_{0.2}Nd_{0.17}MnO_3$(LSNMO) and the effect of *f*-orbitals on the magnetic properties of $La_{0.8}Sr_{0.2}MnO_3$ were investigated by first-principles calculations of density functional theory (DFT). $La_{0.8}Sr_{0.2}MnO_3$ is chosen as the substrate and $La^{3+}$ is replaced by trace amounts of $Nd^{3+}$ to investigate the MCE. Near the $T_c$, $La_{0.63}Sr_{0.2}Nd_{0.17}MnO_3$ (LSNMO) exhibits a significant MCE. The maximum magnetic entropy change ($-\Delta S_M^{max}$) and relative cooling power (RCP) of LSNMO (298 K, 3 T) are 2.70 J/(kg K) and 135 (J/kg), respectively. Thus, it can be concluded that the MCE of the material after doping with *f*-orbital ions ($Nd^{3+}$) is enhanced compared to $La_{0.8}Sr_{0.2}MnO_3$.[28]

## Experimental

LSNMO was prepared by sol–gel (S–G) using $La(NO_3)_3{\cdot}6H_2O$, $Sr(NO_3)_2$, $Mn(NO_3)_2$ (50%), $Nd(NO_3)_3{\cdot}6H_2O$ as raw materials. All chemicals used are the Aladdin brand with ≥ 99.5% purity. The raw material was first dissolved in deionized water with hot stirring at 358 K until a wet gel was formed. Citric acid and ethylene glycol were then added to the solution as complexing and polymerizing agents. The formed wet gel was dried at 394 K for 12 h to obtain a dry gel, which was then placed in a muffle furnace for heat treatment (in order to remove organic matter). Finally, the powder was sintered in a muffle furnace at 1173 K for 12 h to obtain LSNMO.

## Results and Discussion

The LSNMO was characterized by x-ray diffraction (XRD) using CuKα radiation ($\lambda = 1.54059$ Å) to analyze the structure of the LSNMO. The LSNMO was subjected to Rietveld refinement using the GSAS EXPGUI software program. Figure 1a confirms the LSNMO rhombohedral structure of the *R*-3*c* space group (No. 167) ($R_{wp} = 3.91\%$, $R_p = 2.57\%$, $\chi^2 = 3.831$). LSNMO is highly crystalline and does not undergo a structural transformation, but the doping of $Nd^{3+}$ distorts the cell. Doping of $Nd^{3+}$ (1.27 Å) with a smaller ionic radius changes the bond length and bond angle between the Mn ions, causing indirect changes to the Mn–O octahedral structure and a tendency for the cell volume to decrease. The morphology was obtained using scanning electron microscopy (SEM; ZEISS GeminiSEM 300). The microcrystalline size ($D_{XRD}$) of LSNMO was calculated using the Scherrer formula:[29]

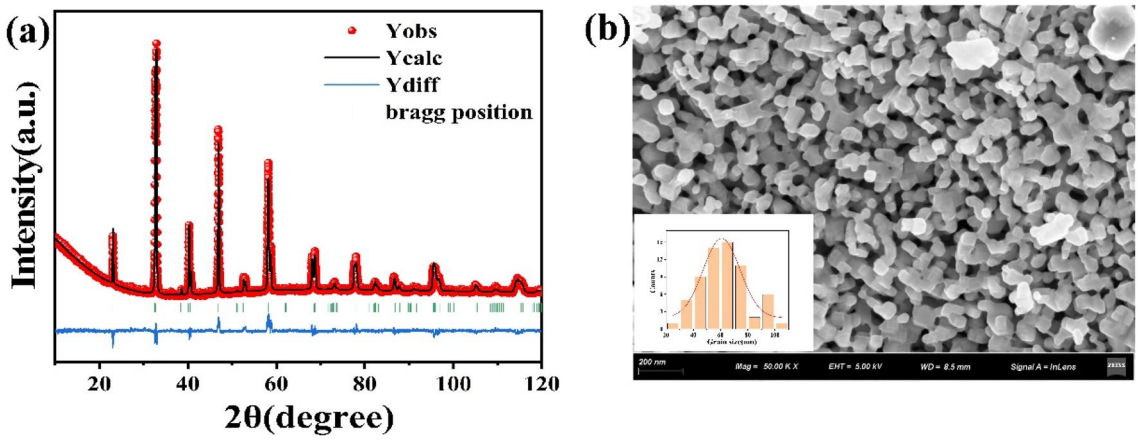


**Fig. 1** (a) XRD with Rietveld refinements of $La_{0.63}Sr_{0.2}Nd_{0.17}MnO_3$. (b) SEM for the LSNMO.

$$D_{XRD} = \frac{K\lambda}{\beta \cos(\theta)}, \quad (1)$$

where $\lambda$, $K$, $\theta$, and $\beta$ indicate the x-ray wavelength, the Scherrer constant ($K = 0.89$), the Bragg diffraction angle, and the half-height width of the LSNMO diffraction peak. The $D_{XRD}$ of LSNMO was calculated as 28.40 nm by Eq. 1. Figure 1b reveals that the LSNMO is composed of nanoscale spherical particles, which appear to be homogeneously dispersed. The average particle size of the LSNMO was 62.69 nm by SEM. The particle size of the LSNMO observed through SEM is much larger than the $D_{XRD}$ obtained from Scherrer's formula, which is illustrated by the fact that each particle is composed of multiple crystallites.[22,30] Figure 2a shows the morphology and structure of LSNMO under transmission electron microscopy (TEM). The LSNMO are nearly spherical particles. Figure 2b displays high-resolution TEM images of LSNMO. Clearly, lattice fringes with regular rhombohedral structure (*R*-3*c* space group, No.167) were observed in the highly crystalline LSNMO.

In this study, the generalized gradient approximation–Perdew–Burke–Ernzerhof (GGA-PBE) exchange–correlation functional[31] in the CASTEP module of the Materials Studio (MS) first-principles computing package is based on DFT for structural calculations. In the LSMO system, the $LaMnO_3$ atoms of the *Pbnm* space group comprising 25 atoms were used as the basic structure, and the La atoms were replaced by two Sr atoms after $1 \times 1 \times 2$ supercell and with 20 Sr and 17 Nd atoms after $2 \times 2 \times 5$ supercell, respectively. In the optimization process, the plane wave cutoff energy was 450 eV, and the energy convergence accuracy was $1 \times 10^{-5}$ eV/atom. The U-values for La, Mn, and Nd were 6.0, 5.0, and 6.0, respectively. We sampled the Brillouin zone using a gamma-centered $3 \times 3 \times 2$ mesh. It was calculated by the LDA+U method.

Figure 3a and b show that the partial densities of the state of $La^{3+}$ and $Sr^{2+}$ are primarily concentrated above $E_f$ and have good symmetry, demonstrating the limited magnetic moments of $La^{3+}$ and $Sr^{2+}$. The results reveal that doping of $Sr^{2+}$ based on $LaMnO_3$ leads to lattice distortion of $La_{1-x}Sr_xMnO_3$, which generates changes in Mn–O bond lengths and bond angles. Figure 3c shows that the spin-up and spin-down electronic states in Mn 3*d* are unsymmetrical, indicating that manganese ions provide a large net magnetic moment for $La_{0.8}Sr_{0.2}MnO_3$ and are the main source of the magnetic properties of $La_{0.8}Sr_{0.2}MnO_3$. Figure 3d illustrates the occurrence of electron exchange and orbital overlap between the Mn 3*d* orbitals and the O 2*p* orbitals, which is a key factor leading to the MCE. Because of the overlap of the Mn 3*d* and O 2*p* orbitals, it can be inferred that $e_g$ itinerant electrons are transported between the Mn and O orbitals near $E_f$.[32,33]

Figure 4a presents the spin-up and spin-down peaks of $La_{0.8}Sr_{0.2}MnO_3$ located on both sides of $E_f$. This confirms the stable magnetic properties of $La_{0.8}Sr_{0.2}MnO_3$ due to the separation of the bonding and antibonding orbitals at $E_f$. The spin-up and spin-down channels display metallic and semiconducting properties, respectively, as can be seen from the $La_{0.8}Sr_{0.2}MnO_3$ total density of states (DOS). Based on the $La_{0.8}Sr_{0.2}MnO_3$, $Nd^{3+}$ is doped at the A-site. According to the DOS of LSNMO, the *f*-orbital of $Nd^{3+}$ provides an efficient pathway for electron transition around the $E_f$ (Fig. 4b). Because of the asymmetry of the *f*-orbital, it provides the net magnetic moment of the LSNMO system. The magnetic entropy of $La_{0.8}Sr_{0.2}MnO_3$ increases after doping with $Nd^{3+}$ in the system.

The MPMS [magnetic property measurement system] (Quantum Design, USA) was adopted for measuring the magnetic features of LSNMO. Figure 5a presents the variation in magnetization (M) of LSNMO at temperatures

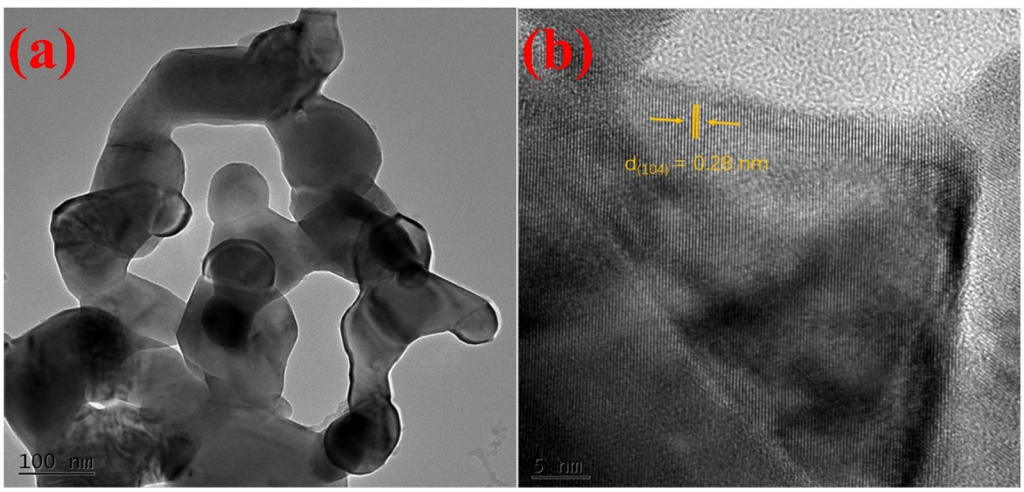


**Fig. 2** (a) TEM images of the $La_{0.63}Sr_{0.2}Nd_{0.17}MnO_3$. (b) The lattice spacing for LSNMO.

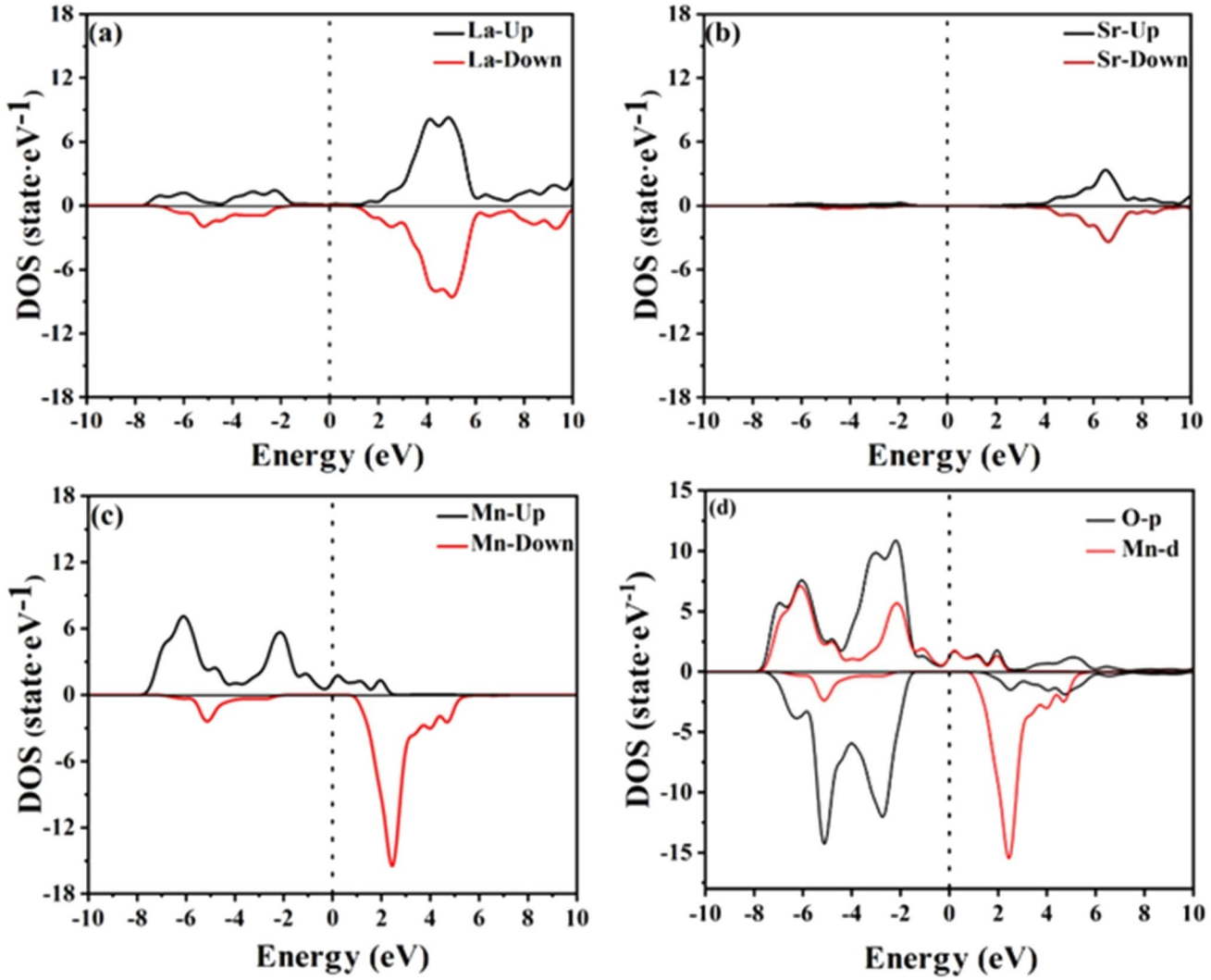


**Fig. 3** Partial density of states of the $La_{0.8}Sr_{0.2}MnO_3$.

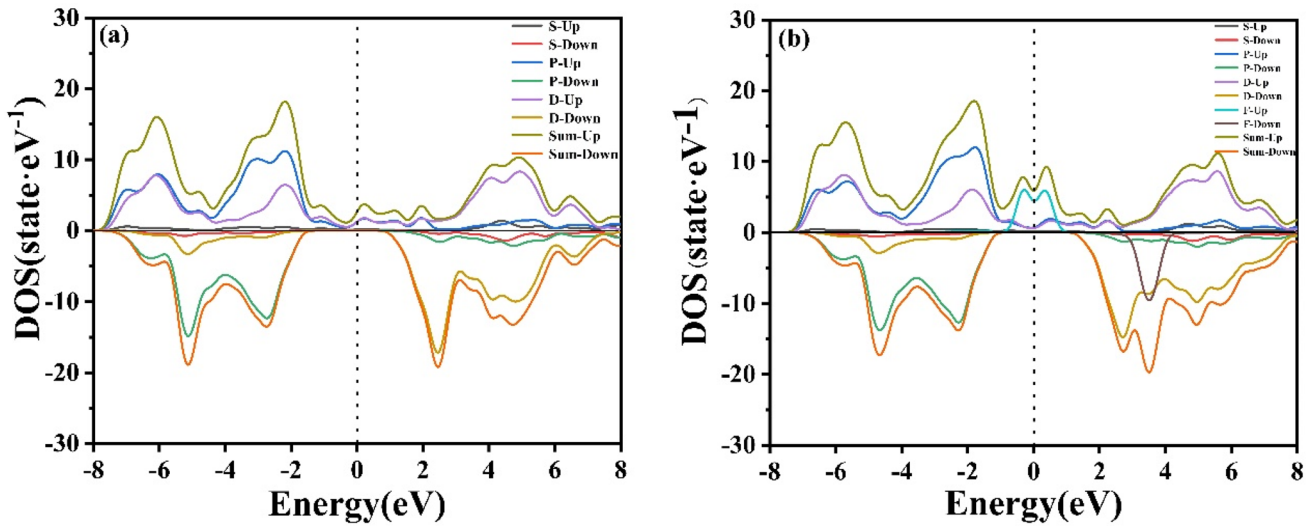


**Fig. 4** (a) Density of states of $La_{0.8}Sr_{0.2}MnO_3$. (b) Density of states of $La_{0.63}Sr_{0.2}Nd_{0.17}MnO_3$.

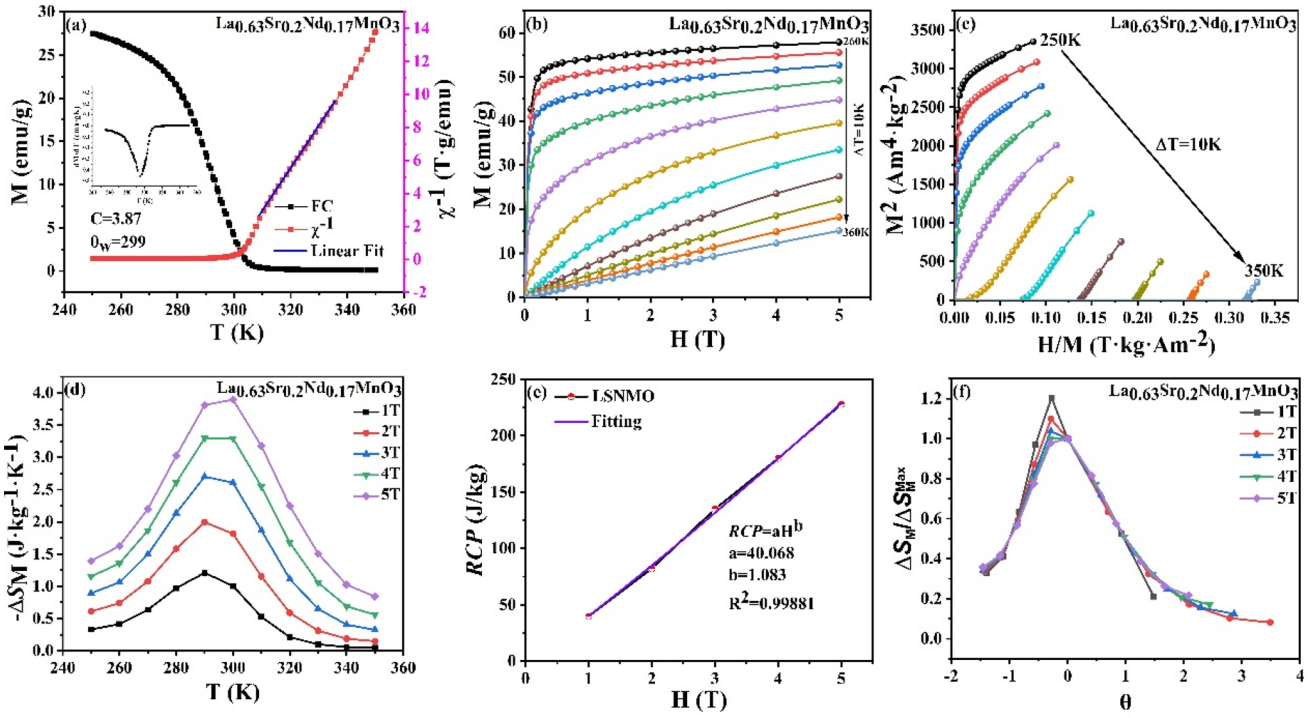


**Fig. 5** (a) Under 0.01 T, the T dependence of the M for LSNMO. The T dependence of the inverse susceptibility at 0.01 T fitted to CW is shown on the right axis. LSNMO dM/dT versus T curve (inset). (b) Isothermal magnetization for LSNMO. (c) Arrott plots of LSNMO. (d) $-\Delta S_M$ versus T curves generated for LSNMO. (e) Fitting results for LSNMO with $RCP = aH^b$. (f) Normalization curves of LSNMO.

ranging from 250 K to 350 K in a magnetic field of 0.01 T. As $T$ decreased, LSNMO underwent a distinct paramagnetic (PM)-to-ferromagnetic (FM) phase transition. The $T_c$ was 298 K for LSNMO as determined by the minimum value of dM/dT at the inflection point of the magnetization curve (inset of Fig. 5a). The Curie–Weiss (C–W) law was used to further investigate the magnetic properties of LSNMO:[34]

$$X = \frac{C}{T - \theta_W}, \tag{2}$$

where $C$ represents the Curie constant of LSNMO and $\theta_w$ denotes the C–W temperature; $\theta_w > T_c$ indicates that FM clusters may exist in the PM phase. After the determination of $C$ from C–W, the experimental effective magnetic moment $\left(\mu_{\text{eff}}^{\text{exp}}\right)$is calculated, which is defined by

$$C = \frac{N_A \mu_B^2}{3K_B} \times \mu_{\text{eff}}^{\text{exp}^2}, \tag{3}$$

where $N_A$ is Avogadro's constant, ($N_A = 6.0232 \times 10^{23}$), and $K_B$ is the Boltzmann constant ($K_B = 1.38016 \times 10^{-23}$ J/K). After $C$ is determined, the experimental effective magnetic moment $\mu_{\text{eff}}^{\text{exp}} = 5.56\ \mu_B$. Meanwhile, the theoretical effective magnetic moment ($\mu_{\text{eff}}^{\text{th}}$) is calculated with the formula[35]

$$u_{\text{eff}}^{\text{th}} = \sqrt{x[\mu(\text{Nd}^{3+})]^2 + 0.8[\mu(\text{Mn}^{3+})]^2 + 0.2[\mu(\text{Mn}^{4+})]^2 u_B}, \tag{4}$$

where $\mu_{\text{eff}}^{\text{th}} = 4.94\ \mu_B$. Since $\mu_{\text{eff}}^{\text{exp}} > \mu_{\text{eff}}^{\text{th}}$, this confirms that FM interactions occur at the PM phase. In order to study the MCE of LSNMO around $T_c$, the dependence of the isothermal magnetization of LSNMO at different $T$ on the magnetic field was measured. The M–$H$ curve of M with $H$ near $T_c$ is shown in the inset of Fig. 5b. LSNMO exhibits FM properties at low temperatures. LSNMO is PM, and M–$H$ is linear when $T > T_c$. As illustrated in Fig. 5b, M–$H$ is not linear with $T > T_c$, confirming the presence of FM clusters in PM and explaining the difference between $\mu_{\text{eff}}^{\text{th}}$ and $\mu_{\text{eff}}^{\text{exp}}$. The $M^2$–$H$/M (Arrott) curve obtained through M–$H$ processing can be used to determine the type of magnetic phase transition of LSNMO (Fig. 5c). The slopes of the Arrott curves are all positive with $T > T_c$ using Banerjee's criterion,[36] confirming that the LSNMO exhibits SOMPT from FM to PM. Because the SOMPT is characterized by an extensive phase transition temperature and lower hysteresis and thermal hysteresis than the primary phase transition process, it is more suitable for obtaining practical LSNMO.

For the discrete field and temperature interval magnetization measurements, $-\Delta S_M$ is approximated by the following equation:[37]

**Table I** A comparison of the $-\Delta S_M^{Max}$, and $T_c$ values of $La_{0.63}Sr_{0.2}Nd_{0.17}MnO_3$ with those of magnetic refrigeration materials reported in previous studies

| Sample | $H$ (T) | $T_c$ (K) | $-\Delta S_{Max}$(J/kg K) | References |
|---|---|---|---|---|
| $La_{0.63}Sr_{0.2}Nd_{0.17}MnO_3$ | 3 | 298 | 2.70 | This work |
| $La_{0.69}Dy_{0.01}Sr_{0.3}MnO_3$ | 3 | 315 | 0.76 | 41 |
| | 5 | 315 | 1.21 | 41 |
| $La_{0.67}Ba_{0.33}MnO_3$ | 5 | 292 | 1.48 | 42 |
| $La_{0.65}Ba_{0.35}MnO_3$ | 5 | 325 | 1.83 | 43 |
| $La_{0.7}Sr_{0.3}MnO_3$ | 5 | 319 | 1.63 | 41 |
| $La_{0.8}Sr_{0.2}MnO_3$ | 2 | 287 | 1.70 | 44 |

$$|\Delta S_M| = \sum_i \frac{M_i - M_{i+1}}{T_{i+1} - T_i} \Delta H_i. \quad (5)$$

The $-\Delta S_M$ of LSNMO increases with increasing $H$ and reaches a maximum around $T_c$ (Fig. 5d) at different $H$, which is consistent with the properties of FM materials. Another important parameter for calculating the MCE[38] is RCP, which can be expressed as

$$\mathrm{RCP} = -\Delta S_{\mathrm{Max}} \times \delta T_{\mathrm{FWHM}}. \quad (6)$$

When $H = 3$ T, $-\Delta S_M^{\mathrm{Max}} = 2.70$ J/(kg K), and RCP = 135 J/kg. The values of $T_c$ and $-\Delta S_M^{\mathrm{Max}}$ for LSNMO are listed in Table I and are compared with the values of other magnetic materials at the same $H$. Figure 5e displays the relationship of the RCP of LSNMO with $H$. The RCP of LSNMO gradually increased with increasing $H$. This suggests a correlation between RCP and $H$. $\mathrm{RCP} = aH^b$, proving that RCP depends on $H$.[39] The value of $b$ is comparable to previously reported values.[4] In addition, normalization can further determine the type of phase transition. When the material is a primary phase transition, the $\Delta S_M$ curve at different $H$ cannot collapse into a $\Delta S_M / \Delta S_M^{\mathrm{Max}}$. It can collapse into a single curve when the material is SOMPT. The equation for the normalization curve is[40]

$$\theta = \begin{cases} (T_c - T)/(T_1 - T_c), (T \le T_c) \\ (T - T_c)/(T_2 - T_c), (T > T_c) \end{cases}. \quad (7)$$

The temperatures $T_1$ and $T_2$ must satisfy the relation $\Delta S_M(T_2) = \Delta S_M(T_1) = \frac{1}{2}\Delta S_M^{Max}$. In Fig. 5f, magnetic entropy curves for LSNMO collapse to a single magnetic entropy curve, with the curves near $T_c$ overlapping the most. This demonstrates that the FM–PM transition of LSNMO is a SOMPT; these findings are consistent with the findings for the Arrott curves.

## Conclusion

In this work, a significant discrepancy between the spin-up and spin-down of the $f$-orbitals of $La_{0.63}Sr_{0.2}Nd_{0.17}MnO_3$ in the −2 eV to 4 eV region of the DOS diagram is revealed using first-principles calculations. This implies that the electronic structure of the Nd atoms exhibits a larger spin polarization on both sides of the Fermi energy level while providing a larger magnetic moment for the material. This suggests that the doping of $Nd^{3+}$ influences the changes in the magneto-thermal properties of the $La_{0.63}Sr_{0.2}Nd_{0.17}MnO_3$ material. The LSNMO was prepared by SG, and its structure, morphology, and MCE were investigated. The samples are pure phases with nanoscale spherical particles, and the PM–FM transition occurs around $T_c$, where the SOMPT of PM–FM occurs, and the PM contains FM clusters. This report can serve as a reference for researchers interested in magnetic refrigeration near $T_c$.

**Acknowledgments** This work was supported by the National Natural Science Foundation of China (No. 52162038).

**Data availability** The datasets generated and analyzed during the current study are available from the corresponding author upon reasonable request.

**Conflict of interest** No conflict of interest exits in the submission of this manuscript, and the manuscript is approved by all authors for publication. The corresponding author declares, on behalf of all co-authors, that the work described was original research that has not been published previously, and is not under consideration for publication elsewhere, in whole or in part. All the authors listed have approved the manuscript.

## References

1. A. Cera-Manjarres, D. Salavera, and A. Coronas, Vapour pressure measurements of ammonia/ionic liquids mixtures as suitable alternative working fluids for absorption refrigeration technology. *Fluid Phase Equilib.* 476, 48 (2018).
2. K.A. Gschneidner Jr. and V.K. Pecharsky, Thirty years of near room temperature magnetic cooling: where we are today and future prospects. *Int. J. Refrig.* 31, 945 (2008).
3. Z.J. Xie, Z.G. Zou, B.R. He, L.L. Liu, and Z. Mao, Research progress of doped manganite materials in magnetic refrigeration. *Front. Mater.* 8, 771941 (2021).
4. M.-H. Phan and S.-C. Yu, Review of the magnetocaloric effect in manganite materials. *J. Magn. Magn. Mater.* 308, 325 (2007).
5. Z.J. Xie, W.J. Zhang, Z.G. Zou, and X.Y. Jiang, Structural, magnetic, magnetocaloric, investigations on $La_{0.8-x}K_xSr_{0.2}Mn_{0.95}Ni_{0.05}O_3$ ($x = 0.05$, 0.10 and 0.15) at room temperature. *J. Magn. Magn. Mater.* 563, 170014 (2022).
6. I. Rasta, I. Susila, I. Subagia, Technology application of environmental friendly refrigeration (green refrigeration) on cold storage for fishery industry, in *Journal of Physics: Conference Series*, vol. 953 (IOP Publishing, 2018), p. 012077.

7. V. Franco, J.S. Blazquez, J.J. Ipus, J.Y. Law, L.M. Moreno-Ramirez, and A. Conde, Magnetocaloric effect: from materials research to refrigeration devices. *Prog. Mater. Sci.* 93, 112 (2018).
8. Y.K. Zhang, Y. Tian, Z.Q. Zhang, Y.S. Jia, B. Zhang, M.Q. Jiang, J. Wang, and Z.M. Ren, Magnetic properties and giant cryogenic magnetocaloric effect in B-site ordered antiferromagnetic $Gd_2MgTiO_6$ double perovskite oxide. *Acta Mater.* 226, 117669 (2022).
9. L.W. Li and M. Yan, Recent progress in the development of RE2TMTM'O6 double perovskite oxides for cryogenic magnetic refrigeration. *J. Mater. Sci. Technol.* 136, 1–12 (2023).
10. J.L. Lin, X. Wang, F.Y. Chen, H.F. Li, and L.W. Li, Designing gadolinium-transition metals-based perovskite type high entropy oxides with good cryogenic magnetocaloric performances. *J. Mater. Sci. Technol.* 207, 317 (2025).
11. Z.P. Ma, P. Xu, J.Y. Ying, Y.K. Zhang, and L.W. Li, Insight into the structural and magnetic properties of RECo12B6 (RE = Ce, Pr, Nd) compounds: a combined experimental and theoretical investigation. *Acta Mater.* 247, 118757 (2023).
12. Y.K. Zhang, W.X. Hao, J.L. Lin, H.F. Li, and L.W. Li, Geometrically frustrated $Gd_2Ti_2O_7$ oxide: a comprehensive exploration of structural, magnetic, and magnetocaloric properties for cryogenic magnetic cooling applications. *Acta Mater.* 272, 119946 (2024).
13. Y.K. Zhang, W.X. Hao, C.L. Hu, X. Wang, X.F. Zhang, and L.W. Li, Rare-earth-free $Mn_{30}Fe_{20-x}Cu_xAl_{50}$ magnetocaloric materials with stable cubic CsCl-type structure for room-temperature refrigeration. *Adv. Func. Mater.* 33, 2310047 (2023).
14. X. Wang, W.X. Hao, N.Z. He, X.H. Wang, Y.K. Zhang, and M. Yan, Structural and cryogenic magnetic properties of the REOCl (RE = Ho, Dy, Tb, and Gd) compounds. *Ceram. Int.* 50, 19838 (2024).
15. Y.K. Zhang, J.Y. Ying, X.Q. Gao, Z.J. Mo, J. Shen, and L.W. Li, Exploration of the rare-earth cobalt nickel-based magnetocaloric materials for hydrogen liquefaction. *J. Mater. Sci. Technol.* 159, 163 (2023).
16. V.A. Chernenko, J.M. Barandiaran, J. Rodriguez Fernandez, D.P. Rojas, J. Gutierrez, P. Lazpita, and I. Orue, Magnetic and magnetocaloric properties of martensitic $Ni_2Mn_{1.4}Sn_{0.6}$ Heusler alloy. *J. Magn. Magn. Mater.* 324, 3519 (2012).
17. A. Chakrabarti and S.R. Barman, Theoretical prediction of shape memory behavior and ferrimagnetism in $Mn_2NiIn$. *Appl. Phys. Lett.* 94, 161908 (2009).
18. C. Moure and O. Pena, Magnetic features in $REMeO_3$ perovskites and their solid solutions (RE = rare-earth, M e= Mn, Cr). *J. Magn. Magn. Mater.* 337, 1 (2013).
19. P. Zhang, H.-G. Piao, Y.-D. Zhang, and J.-H. Huang, Research progress of critical behaviors and magnetocaloric effects of perovskite manganites. *Acta Phys. Sin.* 70, 157501 (2021).
20. K. Laajimi, F. Ayadi, M. Kchaw, I. Fourati, M. Khlifi, M.H. Gazzah, J. Dhahri, and J. Juraszek, A new range of specific perovskite-type materials with structural, magnetic and magnetocaloric properties: $La_{0.67}Ca_{0.33-x}Sr_xMn_{0.98}Fe_{0.02}O_3$ ($0.15 \le x \le 0.3$). *Solid State Sci.* 119, 106683 (2021).
21. A. Barman, S. Kar-Narayan, and D. Mukherjee, Caloric effects in perovskite oxides. *Adv. Mater. Interfaces* 6, 1900291 (2019).
22. P.W. Anderson and H. Hasegawa, Considerations on double exchange. *Phys. Rev.* 100, 675 (1955).
23. M. Zarifi, P. Kameli, M. Mansouri, H. Ahmadvand, and H. Salamati, Magnetocaloric effect and critical behavior in $La_{0.8-x}Pr_xSr_{0.2}MnO_3$ ($x = 0.2, 0.4, 0.5$) manganites. *Solid State Commun.* 262, 20 (2017).
24. F. Cao, H. Chen, Z. Xie, Y. Lu, J. Zhao, and X. Jin, Magnetic properties and magnetic entropy changes of perovskite manganese oxide $La_{0.8-x}Eu_xSr_{0.2}MnO_3$ ($x = 0, 0.075$). *Chin. J. Phys.* 65, 424 (2020).
25. Z.J. Xie, Z.G. Zou, X.Y. Jiang, W.J. Zhang, B.R. He, X.N. Han, and Z. Mao, Structural, magnetic, and magnetocaloric properties of $La_{0.7}Sr_{0.2}Nd_{0.1}Mn_{1-x}Ni_xO_3$ ($x$= 0.05, 0.10, and 0.15): B-site doping. *Phys. B Condens. Matter.* 639, 413985 (2022).
26. W. Xia, K. Leng, Q. Tang, L. Yang, Y. Xie, Z. Wu, K. Yi, and X. Zhu, Structural characterization, magnetic and optical properties of perovskite $(La_{1-x}Ln_x)_{0.67}Ca_{0.33}MnO_3$ (Ln = Nd and Sm; $x = 0.0$-0.5) nanoparticles synthesized via the sol-gel process. *J. Alloys Compd.* 867, 158808 (2021).
27. P. Duan, Z. Chen, S. Dai, L. Liu, and J. Gao, Electrical transport and magnetic properties of perovskite-type electron-doped LaPrMnO epitaxial films. *J. Magn. Magn. Mater.* 301, 521 (2006).
28. A. Lakouader, Y. Hadouch, D. Mezzand, V. Laguta, M. Amjoud, V.O. Dolocan, N. Novak, L. Hajji, E.H. Choukri, A. Razumnaya, A. Alimoussa, Z. Kutnjak, I.A. Luk'yanchuk, and M.E. Marssi, Impact of polymeric precursor and auto-combustion on the structural, microstructural, magnetic, and magnetocaloric properties of $La_{0.8}Sr_{0.2}MnO_3$. *J. Magn. Magn. Mater.* 586, 171225 (2023).
29. C. Kursun, M. Gogebakan, E. Uludag, M.S. Bozgeyik, and F.S. Uludag, Structural, electrical and magnetic properties of Nd-A-$CoO_3$ (A = Sr, Ca) perovskite powders by mechanical alloying. *Sci. Rep.* 8, 13083 (2018).
30. A. Elghoul, A. Krichene, N. Chniba Boudjada, and W. Boujelben, Rare earth effect on structural, magnetic and magnetocaloric properties $La_{0.75}Ln_{0.05}Sr_{0.2}MnO_3$ of manganites. *Ceram. Int.* 44, 12723 (2018).
31. J.P. Perdew, K. Burke, and M. Ernzerhof, Generalized gradient approximation made simple. *Phys. Rev. Lett.* 77(18), 3865 (1996).
32. Z. Zou, S. Zhang, and S. Li, A review of the preparation and performance improvement of $V_6O_{13}$ as a cathode material for lithium-ion batteries. *Mater. Technol.* 35(5), 300 (2020).
33. Y. Zhang, Z. Zou, J. Liu, Effect of Ga doping on structure and properties of $V_2O_5$ lithium-ion batteries. *Mater. Technol.* 1 (2020).
34. P.T. Phong, L.V. Bau, L.C. Hoan, D.H. Manh, N.X. Phuc, and I.-J. Lee, B-site aluminum doping effect on magnetic, magnetocaloric and electro-transport properties of $La_{0.7}Sr_{0.3}Mn_{1-x}Al_xO_3$. *J. Alloy. Compd.* 645, 243 (2015).
35. K.H.J. Buschow and F.R. de Boer, *Physics of Magnetism and Magnetic Materials* (Kluwer Academic/Plenum Publishers, 2003).
36. S.K. Banerjee, On a generalised approach to first and second order magnetic transitions. *Phys. Lett.* 12, 16 (1964).
37. K.A. GschneidnerJr, V.K. Pecharsky, and A.O. Tsokol, Recent developments in magnetocaloric materials. *Rep. Prog. Phys.* 68, 1479 (2005).
38. V. Franco, J.S. Blazquez, B. Ingale, and A. Conde, The magnetocaloric effect and magnetic refrigeration near room temperature: materials and models. *ChemInform* 42, 305 (2012).
39. V. Franco and A. Conde, Scaling laws for the magnetocaloric effect in second-order phase transitions: from physics to applications for the characterization of materials. *Int. J. Refrig.* 33, 465 (2010).
40. C.M. Bonilla, J. Herreroalbillos, F. Bartolome, L.M. Garcia, M. Parraborderias, and V. Franco, Universal behavior for magnetic entropy change in magnetocaloric materials: an analysis on the nature of phase transitions. *Phys. Rev. B* 81, 224424 (2010).
41. I. Sfifir, A. Ezaami, W. Cheikhrouhou-Koubaa, and A. Cheikhrouhou, Structural, magnetic and magnetocaloric properties in $La_{0.7-x}Dy_xSr_{0.3}MnO_3$. *J. Alloy. Compd.* 696, 760 (2017).
42. D. Morelli, A. Mance, J. Mantese, and A. Micheli, Magnetocaloric properties of doped lanthanum manganite films. *J. Appl. Phys.* 79, 373–375 (1996).
43. A.E.M.A. Mohamed, B. Hernando, and A.M. Ahmed, Magnetic, magnetocaloric and thermoelectric properties of nickel doped manganites. *J. Alloy. Compd.* 692, 381 (2017).
44. M. Pkaa and V. Drozd, Magnetocaloric effect in $La_{0.8}Sr_{0.2}MnO_3$ manganite. *J. Alloys Compd.* 456(1–2), 30 (2008).